

Spectral-Spatial Graph Reasoning Network for Hyperspectral Image Classification

Di Wang, *Student Member, IEEE*, Bo Du, *Senior Member, IEEE*, Liangpei Zhang, *Fellow, IEEE*

Abstract—In this paper, we propose a spectral-spatial graph reasoning network (SSGRN) for hyperspectral image (HSI) classification. Concretely, this network contains two parts that separately named spatial graph reasoning subnetwork (SAGR) and spectral graph reasoning subnetwork (SEGRN) to capture the spatial and spectral graph contexts, respectively. Different from the previous approaches implementing superpixel segmentation on the original image or attempting to obtain the category features under the guide of label image, we perform the superpixel segmentation on intermediate features of the network to adaptively produce the homogeneous regions to get the effective descriptors. Then, we adopt a similar idea in spectral part that reasonably aggregating the channels to generate spectral descriptors for spectral graph contexts capturing. All graph reasoning procedures in SAGR and SEGRN are achieved through graph convolution. To guarantee the global perception ability of the proposed methods, all adjacent matrices in graph reasoning are obtained with the help of non-local self-attention mechanism. At last, by combining the extracted spatial and spectral graph contexts, we obtain the SSGRN to achieve a high accuracy classification. Extensive quantitative and qualitative experiments on three public HSI benchmarks demonstrate the competitiveness of the proposed methods compared with other state-of-the-art approaches.

Index Terms—Adaptively, non-local self-attention mechanism, spectral-spatial graph reasoning network (SSGRN), hyperspectral image (HSI) classification

I. INTRODUCTION

Relying on the excellent characteristics that the intrinsic properties of the targets can be identified by automatically extracting the effective features in an end-to-end manner. The deep learning technologies are being extensively employed in processing of the hyperspectral image (HSI). The HSI includes abundant spectral information which is carried by hundred of bands and vision representations presented by high spatial resolution, effectively serving the precision agriculture [1], environmental monitoring [2], anomaly detection [3] and so on. Among these fields, the land cover classification is always a fundamental and hot topic, where each pixel in the whole scene is needed to be assigned a certain and unique semantic category.

In early HSI classification community, the deep features are usually obtained with the networks of fully connected structure [4]–[6]. For example, Chen et al. [4] directly uses the

stacked autoencoder (SAE) to extract the spectral and spatial features, respectively. They adopt the layer-wise stacked pre-training strategy to ensure the stability of network learning and progressively deepen the networks, while Li et al. [5] employs another deep neural network (DNN) called belief network based on the restricted Boltzmann machine to classify the HSI. However, these networks require sufficient computations since each neuron needs to connect with all the units in next layer, demanding to optimize a large amount of parameters, and inevitably generates the overfitting phenomenon. In addition, the input form is strictly restricted that only the 1-D data can be fed into the networks. Thus, in order to obtain the spatial information, Chen et al. has to flatten the image patches to fit the SAE, and the spatial structures are unavoidably destroyed, affecting the classification accuracy.

To tackle these problems, in recent years, many researchers begin to interpret the HSI for pixel-level classification using convolutional neural networks (CNNs), where the fixed size convolution kernels slide on the whole image and the corresponding parameters are constantly updated according to the global statistical characteristics. Thus, compared with DNNs receiving 1-D spectral vectors, the CNNs that process the clipped spatial patches around the target pixel have larger vision fields since they can perceive the neighborhood information of the target pixel and reduce the overfitting because there are fewer parameters needed to be learned. In the past years, regarding the abundant spectral channels in HSI, the mainstream deep learning-based HSI parsing methods are all on the foundation of classification networks, where the output is a group of category probability vector and the input is mainly spatial patches or spectral vectors of the target pixel. For example, Hu et al. [7] extracts the spectral features with a five layer 1-D CNN. In [8], the 2-D CNN is utilized to obtain spatial features, while the spectral-spatial joint features are acquired in [9]–[12]. In addition to being directly used as an extractor for single scale feature, the architectures of CNN can be modified to generate the enhanced features for further accuracy improving [13]–[23].

However, as the networks deepen, their abilities are soon saturated since the limited size of input patches in spite of possess an extraordinarily large theoretical receptive field. To this end, many fully convolutional network (FCN) based deep learning methods are recently developed, where the whole image can be directly input into the network and simultaneously classify all pixels. With the FCN, it's naturally consider stacking the convolutional layers to increase the receptive field [24]–[27]. Specifically, in [24], the dilated convolution is used in spatial part to expand the vision field. However, the ordinary

Corresponding authors: Bo Du; Liangpei Zhang.

D. Wang and B. Du are with the School of Computer Science, Wuhan University, Wuhan 430072, China (e-mail: wd74108520@gmail.com; gun-space@163.com).

L. Zhang is with the State Key Laboratory of Information Engineering in Surveying, Mapping and Remote Sensing, Wuhan University, Wuhan 430079, China (e-mail: zlp62@whu.edu.cn).

and dilated convolution are all local operators, meaning it is still difficult to model the dependence between a specific pixel and other long-range positions, thus the networks can't fully leverage the contexts.

In order to capture the non-local contexts, [28] firstly introduces the self-attention [29] mechanism into computer vision field. They compute the similarity between spatial points in a projected latent semantic space and aggregate these points by weighted addition. Then, [30] and [31] perform the scene parsing of natural image by directly regarding the pixel as the spatial points, where each pixel has a global view of the image. However, these networks inevitably have high computational complexity since each pixel need to compute the similarity with all the other pixels, requiring $\mathcal{O}(N^2)$ calculations, where $N = HW$ is the pixel number, H and W are height and width. To shrink the computations, [32] only captures the contexts in same row or column, decreasing the complexity to $\mathcal{O}(N\sqrt{N})$ since usually $H = W = \sqrt{N}$, while the complexity in [33] is $\mathcal{O}(NP)$, where P is the remaining pixel number after conducting pyramid pooling [34]. But the straightforward pyramid pooling neglects the intrinsic information in image, so [35] and [36] obtain the district features through combining the contexts in a same category under the guide of ground truth. However, they have to use the coarse segmentation mask when inferring without the truth label, bringing the unnecessary errors. Different from these approaches, the descriptors in our methods are the gathering centers obtained by separately aggregating the features in the homogeneous areas. Concretely, these areas are generated by superpixel segmentation that based on the pixel spectral-spatial similarities [37], [38]. Thus, the proposed methods not only require a lower complexity compared with the original non-local module, but produces the more effective descriptors since the homogeneous regions can be adaptively obtained whether in training or testing.

It should be noticed that the input and output of HSI classification task are similar with the semantic segmentation of natural image, meaning some patterns in natural image segmentation field may still play a role for HSI classification. However, different from the rich and complex natural image database which has certain channels, HSI scene usually involves only a single image with hundreds of bands that are determined with the sensor type. Thus, one of the key parts in HSI processing can be distinguished from the natural image operation is to explore how to better exploit the rich spectral information. In fact, the adjacent bands in HSI contain contextual information [14], [15]. Thus, we adopt a similar idea that reasonably aggregating the channels to generate spectral descriptors for better spectral contexts capturing.

The conventional CNN only aggregate the contexts in a regular region. However, the objects in images usually have an irregular distribution. Therefore, it is unsuitable to place these spatial descriptors in a form of regular grid. It is more appropriate to solve this problem from graph perspective where each descriptor is considered as a graph node. Then the graph contexts can be well extracted by conducting graph convolutional network (GCN) [39], which is first implemented in a transductive pattern where each pixel is regarded as a node and the whole image need to be fed into the network,

requiring a large amount of computing resource. There are two solutions to address this problem, one is inductive learning, which is attempt to achieve this procedure using mini-batch training strategy [40], while another is with the representative descriptors because of the redundant information lying in adjacent pixels. For example, [41] generates the descriptors by directly segmenting the original image using superpixel and obtains the multiscale features through combining the node contexts in different neighborhoods, corresponding to different adjacent matrices, and performs the superpixel-level labeling. [42] further optimizes the adjacent matrices producing procedure with the generalized mahalanobis distance and constructs the projection matrix to implement the mapping of pixel to region and region to pixel. Different from above approaches, we generate the descriptors based on the intermediate features in network, thus our methods can adaptively produce the more flexible homogeneous areas for the more powerful descriptors obtaining. In addition, we conduct the graph reasoning based on the similarities between the descriptors in a global view to acquire the more effective graph contexts. This can be implemented with the help of self-attention mechanism. What's more, besides the spatial graph reasoning, we also implement the graph convolution on the spectral descriptors to capture the relationships of different spectral channels. To our best knowledge, it is the first time to put the superpixel segmentation procedure into network for training in an end-to-end manner and implement graph reasoning between spectral bands for HSI classification.

We call our method as spectral-spatial graph reasoning network (SSGRN), which includes the spatial graph reasoning subnetwork (SAGRn) and spectral graph reasoning subnetwork (SEGRn), the main contributions of this paper can be summarized as follows:

- 1) We propose an end-to-end spectral-spatial graph reasoning network named SSGRN. Compared with existing spectral-spatial joint networks, our model can adaptively capture the inter-relationship of the representative descriptors and fully exploit the graph contexts.
- 2) To generate the effective descriptors, we design the spatial subnetwork SAGRn, where the homogeneous areas are adaptively generated by involving the superpixel segmentation procedure into network and training in an end-to-end manner.
- 3) A spectral subnetwork SEGRn is proposed to capture the contextual information lying in different bands using graph reasoning. As far as we know, it is the first time the relationships of spectral channels are explored from graph perspective for HSI classification.
- 4) Benefitting from the proposed graph reasoning modules. Our networks yield significant improvement in three HSI classification benchmarks compared with other GCN-based methods.

The remainder of this paper is organized as follows. Section II gives an introduction of related works. Section III describes the proposed networks. Experiments and related comprehensive analyses are presented in section IV. Finally, Section V concludes this paper.

II. RELATED WORK

A. Semantic Segmentation for Natural Image

Since the fully convolutional networks are used by FCN [43] for semantic segmentation into natural scene, the FCN-based methods keep making progress. UNet [44], SegNet [45], DeconvNet [46], RefineNet [47] and DFNet [48] adopt encoder-decoder architectures to carefully recover the details in upsampling procedure. To perceive the global information, GCN [49] uses the larger kernel, BiSeNet [50] adopts the global pooling, while an effective encoding layer is introduced in EncNet [51] on top of the network. There are also some networks extracting the features from the perspective of categories [35], [36]. In the aspect of multiscale feature generating, multiple atrous convolution filters are employed in DeeplabV3 [52] to construct the ASPP module to regularly capture the objects in different range of the target pixel. DenseASPP [53] further increases the receptive field with the dense connection while PSPNet [34] parallel meshes the feature map to different size using the PPM module. ACFNet [36] and [35] use the features of same category to produce descriptors. Different with them, our SAGRN obtains the descriptors by gathering the features in homogeneous areas that generated with superpixel segmentation, and we further enhance the descriptors through capturing the graph contexts of them. In addition, considering the abundant spectral information in HSI, in SEGRN, we also implement the graph reasoning to obtain the relationships between channels.

B. Graph Convolutional Network

According to the convolution theorem, for functions f, g

$$\mathcal{F}(f \star g) = \mathcal{F}(f) \cdot \mathcal{F}(g) \quad (1)$$

Thus, the convolution operation can be rewritten as

$$f \star g = \mathcal{F}^{-1}(\mathcal{F}(f) \cdot \mathcal{F}(g)) \quad (2)$$

where \mathcal{F} and \mathcal{F}^{-1} are fourier transform (FT) and inverse fourier transform (IFT), meaning the graph convolution \mathcal{G} of filter g and node x in graph G is the multiplication in transformed fourier domain

$$\mathcal{G}(g \star x) = \mathcal{F}^{-1}(\mathcal{F}(g) \cdot \mathcal{F}(x)) \quad (3)$$

In fact, the basis of FT is the eigenvectors that make up the orthogonal matrix (spectral matrix) which is produced by implementing the spectral decomposition (SD) \mathcal{D} on the laplacian matrix L_G of graph G , which is defined as

$$L^G = D^G - A^G \quad (4)$$

where D^G and A^G are the degree matrix and adjacency matrix, $D_{ii}^G = \sum_{j=1}^K A_{ij}^G$. K is the nodes number. Actually, the symmetric normalized laplacian matrix \tilde{L}^G is more commonly used in GCN

$$\tilde{L}^G = \frac{-1}{\sqrt{D^G}} L^G \frac{-1}{\sqrt{D^G}} = I_K - \frac{-1}{\sqrt{D^G}} A^G \frac{-1}{\sqrt{D^G}} \quad (5)$$

I_K is the identity matrix. Then the SD on \tilde{L}^G is

$$\mathcal{D}(\tilde{L}^G) = U \tilde{\Lambda} U^{-1} = U \tilde{\Lambda} U^T \quad (6)$$

since $U = \{u_1, u_2, \dots, u_K\}$ is the orthogonal spectral matrix ($UU^T = I_K$) and $u_i, i = 1, \dots, K$ are the FT basis. Thus, U^T and U can be regarded as the discrete form of FT and IFT. $\tilde{\Lambda}$ is the diagonal matrix of eigenvalues. Therefore, the equation (3) can be presented as

$$\mathcal{G}(g \star x) = U((U^T g) \cdot (U^T x)) = U g_{\theta}(\tilde{\Lambda}) \cdot (U^T x) \quad (7)$$

where $U^T g$ is the filter that need to be trained and can be considered as the function of $\tilde{\Lambda}$ since the eigenvalues are corresponding to the frequencies of fourier domain.

Implementing equation (7) needs high computational complexity that mainly lying in computing the multiplication of U and eigenvalue decomposition. In practice, the $g_{\theta}(\tilde{\Lambda})$ is approximated by k th truncated expansion of chebyshev polynomials [54].

$$g_{\theta}(\tilde{\Lambda}) \approx \sum_{i=0}^k \theta'_i T_i(\tilde{\Lambda}) \quad (8)$$

where θ' is the chebyshev coefficients. $\tilde{\Lambda} = \frac{2}{\lambda_{max}} \tilde{\Lambda} - I_K$ and λ_{max} is the maximum value in $\tilde{\Lambda}$. In addition, it's obvious that

$$\mathcal{G}(g \star x) \approx \sum_{i=0}^k \theta'_i T_i(\tilde{L}^G) x \quad (9)$$

where $\tilde{L}^G = \frac{2}{\lambda_{max}} \tilde{L}^G - I_K$ since $(U \tilde{\Lambda} U^T)^k = U \tilde{\Lambda}^k U^T$. It can be seen that the graph convolution $\mathcal{G}(\cdot)$ depends on the k th-order neighborhoods since the scaled laplacian matrix \tilde{L}^G is conducted k times, while the largest eigenvalue in $\tilde{\Lambda}$ is 1.

The chebyshev polynomial $T(\cdot)$ is defined in recursion form

$$T_i(x) = \begin{cases} 1, & i = 0 \\ x, & i = 1 \\ 2xT_{i-1}(x) - T_{i-2}(x), & i > 1 \end{cases} \quad (10)$$

To simplify the computation, limiting $i = 1$, $\lambda_{max} = 2$ and $\theta = \theta'_0 = -\theta'_1$ to approximate the graph convolution $\mathcal{G}(g \star x)$ as the linear function of laplacian matrix \tilde{L}^G , when combining equation (5) then the graph convolution

$$\begin{aligned} \mathcal{G}(g \star x) &= \theta'_0 x + \theta'_1 \tilde{L}^G x \\ &= \theta'_0 x + \theta'_1 (\tilde{L}^G - I_K) x \\ &= \theta'_0 x - \theta'_1 \left(\frac{-1}{\sqrt{D^G}} A^G \frac{-1}{\sqrt{D^G}} \right) x \\ &= \theta \left(I_K + \frac{-1}{\sqrt{D^G}} A^G \frac{-1}{\sqrt{D^G}} \right) x \end{aligned} \quad (11)$$

However, the eigenvalues of $I_K + \frac{-1}{\sqrt{D^G}} A^G \frac{-1}{\sqrt{D^G}}$ are in range $[0, 2]$, which may causes gradient explode or vanish when repeating this operation. Thus, [39] gives a renormalization trick that set $\hat{A} = A^G + I_K$, $\hat{D}_{ii} = \sum_{j=1}^K \hat{A}_{ij}$ and the GCN can be formulized as

$$\mathcal{G}^{(l+1)} = \begin{cases} X, & l = -1 \\ \sigma(Z \mathcal{G}^{(l)} W^{(l)}), & l > -1 \end{cases} \quad (12)$$

where X is the original input, $Z = \frac{-1}{\sqrt{\hat{D}}} \hat{A} \frac{-1}{\sqrt{\hat{D}}}$, $\mathcal{G}^{(l)}$ and $W^{(l)}$ are the output and trainable parameter matrix in l th layer, σ is the activation function and the ReLU is used in this paper.

III. PROPOSED METHODS

From the introduction of GCN, it can be seen that the critical parts for graph reasoning are attempt to obtain the Z and X in a more effective way, and this idea will be applied to all parts in the proposed methods.

A. Spatial Graph Reasoning Subnetwork

The hundreds of bands and high spatial resolution in HSI provide strong spectral-spatial relationships of the pixels, and these contextual information is easily utilized with superpixel segmentation, which can be implemented by adopting the SLIC algorithm [55] to generate a series compact superpixels. The original SLIC algorithm is difficult to be directly placed into the network for end-to-end training since the existing undifferentiable min-max operations. [56] addresses this problem by transforming this operation to the differentiable weighted addition. With this technique, we successfully obtain the superpixels inside the network and generate the more effective descriptors. In addition, it can be noticed that the generated superpixels have brought the graph structure and the number of clustered districts is significantly less than the original pixels, benefitting to conduct the graph reasoning in a high efficiency.

In SAGRN, the obtained superpixels and descriptors are in fact the homogeneous regions and $D = \{d_1, d_2, \dots, d_K\} \in \mathbb{R}^{K \times C}$, then the $X = \{x_1, x_2, \dots, x_K\}$ can be easily obtained from D using linear mapping. Concretely, each descriptor is computed through taking the mean value of the features in the corresponding area. This procedure is shown as follows

$$\begin{aligned} S &= \mathcal{S}(F) \\ d_i &= \frac{\sum_{j=1}^{HW} \mathbb{I}(S_j = i) \cdot F_j}{\sum_{j=1}^{HW} \mathbb{I}(S_j = i)} \quad i = 1, \dots, K \\ x_i &= \xi(d_i) \end{aligned} \quad (13)$$

where $F \in \mathbb{R}^{C \times H \times W}$ is the input feature, S and S represent the superpixel generating procedure and the corresponding segmentation result map. There are a total of K descriptors and i is the index, C , H and W are separately the number of channels, height and width of F . $\mathbb{I}(S_j = i)$ is the binary indicator that judges whether the value of j th pixel in S equal to i . ξ represents the 1×1 convolutional layer, which is used to conduct the information integration of different channels.

To obtain Z , different from the conventional adjacent matrix that only considers the neighbor nodes, we treat it as a dense graph that each node possesses the relationship with all the other nodes to better capture the graph contexts. Specifically, the relationship of each pair of nodes is measured by computing their similarity in a mapped latent space

$$Z_{ij} = \frac{\exp(\phi(d_i)^T \psi(d_j))}{\sum_{k=1}^K \exp(\phi(d_i)^T \psi(d_k))} \quad i = 1, \dots, K \quad (14)$$

where ϕ and ψ are the mapping functions, which all can be implemented with the 1×1 convolution. Then, we normalize the similarity matrix using softmax function.

After obtaining the $Z \in \mathbb{R}^{K \times K}$ and $X \in \mathbb{R}^{K \times C_1}$, the spatial graph reasoning is achieved by directly adopting the GCN formula

$$\mathcal{G}(Z, X) = \sigma(ZXW) \quad (15)$$

where $W \in \mathbb{R}^{C_1 \times C_2}$ is the trainable parameters and the ReLU is used as the activation function σ . It can be seen that each district-level feature is enhanced since it has the global view that capturing the contextual information lying in all the other nodes.

At last, these enhanced nodes need to be reprojected for recovering the shape of a pixel-level feature. In fact, the construction of pixel-level feature depends on the combination of reasonable descriptors since they possess specific connotations various from each other. In this paper, the node vectors after reasoning are considered as a group of bases which can span an effective feature space, where the information in any point can be inferred based on the linear aggregation of these vectors for the more complex semantic understanding. To this end, assume $G = \mathcal{G}(Z, X) = \{g_1, g_2, \dots, g_K\} \in \mathbb{R}^{K \times C_2}$, $F = \{f_1, f_2, \dots, f_{HW}\}$, the affinities $A \in \mathbb{R}^{K \times HW}$ between feature F and node set G are firstly measured in a new transformed space

$$A_{ij} = \frac{\exp(\rho(g_i)^T \eta(f_j))}{\sum_{h=1}^{HW} \exp(\rho(g_i)^T \eta(f_h))} \quad i = 1, \dots, K \quad (16)$$

Then the target pixel-level feature $F_{sa_main} \in \mathbb{R}^{HW \times C_3}$ is subsequently obtained by linearly combining these descriptors, where the affinity matrix A is served as the corresponding weights. Thus, $F_{sa_main} = A^T \zeta(G)$, and we subsequently reshape F_{sa_main} to $\mathbb{R}^{C_3 \times H \times W}$. Here, ρ , η and ζ are implemented with 1×1 convolution and the subscript *main* means the main branch to distinguish the later introduced auxiliary path in network. In above procedure, $C = C_1 = C_2 = C_3$ for convenience. After obtaining the F_{sa_main} , through a 3×3 convolutional layer followed by a group normalization (GN) layer, a ReLU function, a 1×1 convolutional layer and a bilinear upsampling function, the probability matrix $P_{sa_main} \in \mathbb{R}^{C_n \times H \times W}$ is acquired for computing loss, where C_n is the number of categories. This procedure is symbolized as follows.

$$P_{sa_main} = \delta_{sa_main}(F_{sa_main}) \quad (17)$$

However, in the early stage of training, the disorganized high-level features may unfavorable to the homogeneous region generating, and the classification quality is suffered with the affected descriptors. To produce the more stable superpixels, we add an auxiliary branch to achieve a fast convergence and obtain the corresponding probability matrix P_{sa_aux} in a similar way as the main branch.

$$P_{sa_aux} = \delta_{sa_aux}(F) \quad (18)$$

In the proposed methods, the loss function is defined to $L_{(\cdot)} = l(P_{(\cdot)}, Y)$, where Y is the ground truth and l is implemented with the cross entropy loss, thus the total loss of SAGRN is

$$L_{sa} = L_{sa_main} + L_{sa_aux} \quad (19)$$

The diagram of SAGRN is presented in Figure 1 (a).

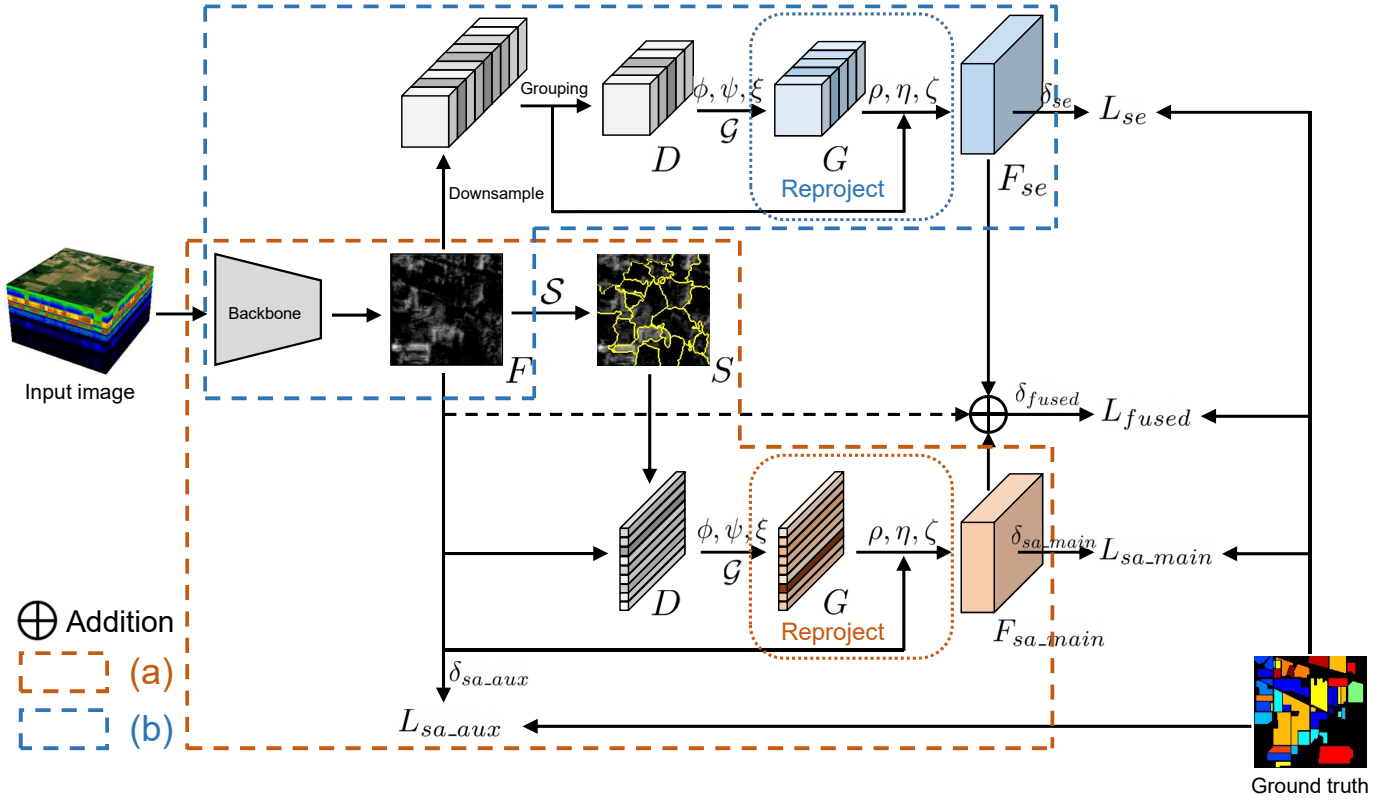


Fig. 1. Architecture of the proposed SSGRN. Firstly, the feature F is obtained after the received image through the backbone network. Then the F is separately fed into two parts of (a) SAGR and (b) SEGR. In spatial part, a superpixel map S is firstly generated based on F and used to produce the descriptor set D . Then a graph convolution is conducted within D and the generated G is employed to reconstruct the pixel-level feature F_{sa_main} under the guide of F for classification. An auxiliary branch is imposed on F to improve the quality of S . In spectral subnetwork, to obtain the pixel-level feature F_{se} , grouping, gradient convolution and reconstruction are sequentially implemented on the foundation of the downsampled F . In the end, a skip connection is built on F to aggregate with F_{sa_main} and F_{se} for final classification.

B. Spectral Graph Reasoning Subnetwork

In SEGRN, we adopt the similar thinking as SAGR. The homogeneous areas in SAGR are regarded as the clustering of pixels. Thus, it is natural to consider aggregating the channels in a reasonable way. In order to obtain the spectral descriptors, inspired by [14], [15], we directly take the mean value of the aggregated features in channel direction, which are realized by grouping the feature maps of adjacent bands.

For the input feature $F' \in \mathbb{R}^{C \times H' \times W'}$ with C bands: $F' = \{b_1, b_2, \dots, b_C\}$, assume they are separately assigned to M groups $F' = \{r_1, r_2, \dots, r_M\}$, then the i th group

$$r_i = \{b_{\frac{C}{M}(i-1)+1}, b_{\frac{C}{M}(i-1)+2}, \dots, b_{\frac{C}{M} \cdot i}\} \quad (20)$$

Thus the i spectral descriptor can be obtained through

$$d_i = \frac{\sum_{j=1}^{C/M} b_{\frac{C}{M}(i-1)+j}}{C/M} \quad (21)$$

The remaining steps are similar with SAGR. It should be noticed that the F' is downsampled from F with average pooling before conducting graph reasoning to save the computing resources. Therefore, $H' < H, W' < W$, and we group the downsampled F' to generate the spectral descriptors. The pixel-level feature $F_{se} \in \mathbb{R}^{C \times H \times W}$ is reconstructed after reasoned descriptor linear combination and the bilinear interpolation is employed to guarantee the feature

sizes are aligned for later aggregation. Through SEGRN, we successfully perform the graph reasoning in spectral direction since the contextual information lying in different channels is perceived and obtain an enhanced feature where each channel is improved by capturing the relationships with other bands. At last, the loss of SEGRN is computed by

$$L_{se} = l(\delta_{se}(F_{se}), Y) \quad (22)$$

The diagram of SEGRN is depicted in Figure 1 (b).

C. Spectral-Spatial Graph Reasoning Network

The feature F is obtained through the backbone network composing with three blocks. Each block includes a convolutional layer followed by a GN layer and a ReLU function. There is 2x downsampling after the first block to reduce the memory consumption. The whole network is trained from the scratch and no pre-trained parameters of the existing popular models need to be loaded.

After passing through the SAGR and SEGRN, we obtain the corresponding enhanced features F_{sa_main} and F_{se} . To preserve the original information, we adopt the residual skip connection, thus the spectral-spatial fused feature $F_{fused} \in \mathbb{R}^{C \times H \times W}$ is defined as

$$F_{fused} = F_{sa_main} + F_{se} + F \quad (23)$$

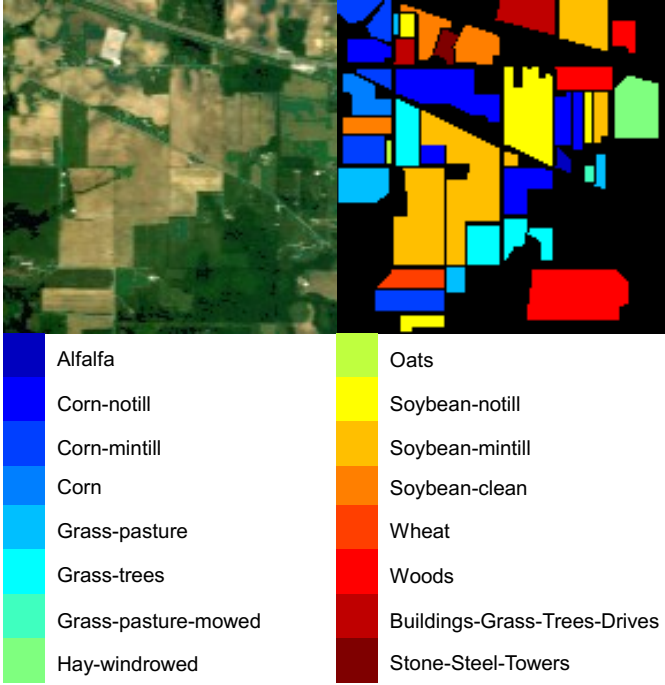


Fig. 2. False color image and ground truth on Indian Pines dataset.

TABLE I
CATEGORY AND SAMPLE SETTING ON INDIAN PINES DATASET

Class ID	Category	Training	Validation	Testing	Total
1	Alfalfa	26	7	13	46
2	Corn-notill	80	20	1328	1428
3	Corn-mintill	80	20	730	830
4	Corn	80	20	137	237
5	Grass-pasture	80	20	383	483
6	Grass-trees	80	20	630	730
7	Grass-pasture-mowed	16	4	8	28
8	Hay-windrowed	80	20	378	478
9	Oats	11	3	6	20
10	Soybean-notill	80	20	872	972
11	Soybean-mintill	80	20	2355	2455
12	Soybean-clean	80	20	493	593
13	Wheat	80	20	105	205
14	Woods	80	20	1165	1265
15	Buildings-Grass-Trees-Drives	80	20	286	386
16	Stone-Steel-Towers	60	15	18	93
Total		1073	269	8907	10249

And the corresponding loss is also obtained

$$L_{fused} = l(\delta_{fused}(F_{fused}), Y) \quad (24)$$

At last, the total loss of the proposed SSGRN is computed by

$$L_{ss} = L_{sa} + L_{se} + L_{fused} \quad (25)$$

The whole diagram of SSGRN is shown in Figure 1.

IV. EXPERIMENTS

In this section, we first introduce the datasets and implementation details, then we conduct a series of qualitative and quantitative comprehensive analyses. The comparison between the proposed methods with other state-of-the-art approaches will be presented in the end.

A. Dataset

- 1) Indian Pines: This scene was gathered at North-western Indiana by Airborne Visible/Infrared Imaging Spectrometer (AVIRIS) sensor in 1992, consisting 200 bands with

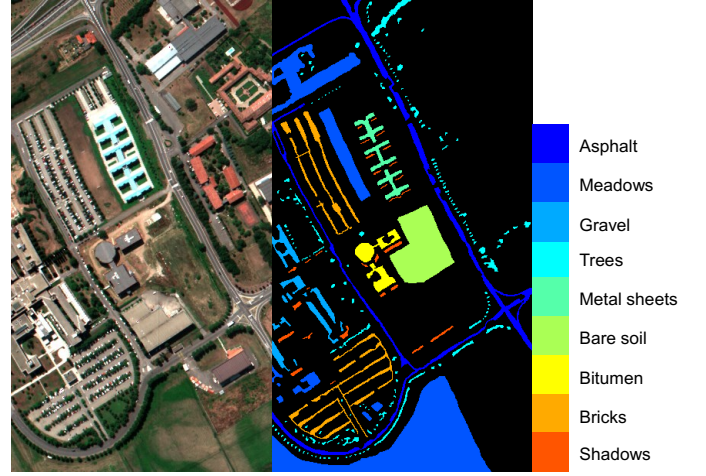


Fig. 3. False color image and ground truth on Pavia University dataset.

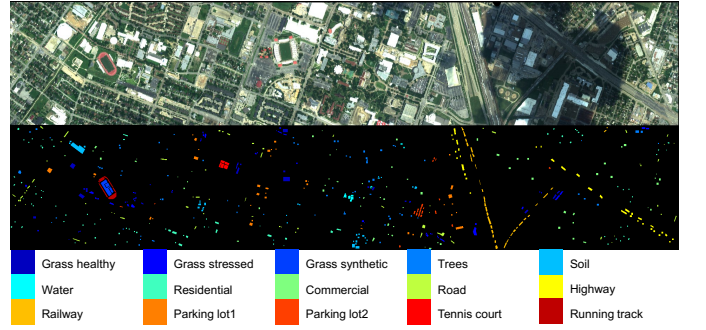


Fig. 4. False color image and ground truth on University of Houston dataset.

size of 145×145 pixels that in 20m spatial resolution after water absorption bands were removed and in the wavelength range of $0.4\text{-}2.5\mu\text{m}$. 16 vegetation classes are involved in this scene, related information such as original image visualization, ground truth, configuration of training, validation and testing samples has been presented in Figure 2 and Table I.

- 2) Pavia University: This scene was obtained over Pavia University at Northern Italy by Reflective Optics System Imaging Spectrometer (ROSIS) in 2001, consisting 103 bands with size of 610×340 pixels that in 1.3m spatial resolution and in the wavelength range of $0.43\text{-}0.86\mu\text{m}$. 9 categories are included in this data, which is shown in Figure 3 and Table II.
- 3) University of Houston: This scene was acquired over the University of Houston campus and its neighbor regions by ITRES-CASI 1500 sensor in 2012, containing 144 bands with size of 349×1905 pixels that in 2.5m spatial resolution and in the wavelength range of $0.4\text{-}1.0\mu\text{m}$. 15 categories are included in this data, which is depicted in Figure 4 and Table III. This scene was also used in the 2013 IEEE GRSS Data Fusion Contest.

B. Implementation Details and Experimental Settings

We employ Pytorch to implement these methods. The base learning rate is set to $1e\text{-}3$, which is adaptively ad-

TABLE II
CATEGORY AND SAMPLE SETTING ON PAVIA UNIVERSITY DATASET

Class ID	Category	Training	Validation	Testing	Total
1	Asphalt	80	20	6531	6631
2	Meadows	80	20	18549	18649
3	Gravel	80	20	1999	2099
4	Trees	80	20	2964	3064
5	Metal sheets	80	20	1245	1345
6	Bare soil	80	20	4929	5029
7	Bitumen	80	20	1230	1330
8	Bricks	80	20	3582	3682
9	Shadows	80	20	847	947
Total		720	180	41876	42776

TABLE III
CATEGORY AND SAMPLE SETTING ON UNIVERSITY OF HOUSTON DATASET

Class ID	Category	Training	Validation	Testing	Total
1	Grass healthy	80	20	1151	1251
2	Grass stressed	80	20	1154	1254
3	Grass synthetic	80	20	597	697
4	Trees	80	20	1144	1244
5	Soil	80	20	1142	1242
6	Water	80	20	225	325
7	Residential	80	20	1168	1268
8	Commercial	80	20	1144	1244
9	Road	80	20	1152	1252
10	Highway	80	20	1127	1227
11	Railway	80	20	1135	1235
12	Parking lot1	80	20	1134	1234
13	Parking lot2	80	20	369	469
14	Tennis court	80	20	328	428
15	Running track	80	20	560	660
Total		1200	300	13511	15011

justed with the poly scheduling strategy and multiplied with $(1 - \frac{iter}{max_iter})^{0.9}$. The SGD with momentum optimizing algorithm is used for training, where the momentum is set to 0.9 and the weight decay is configured as 0.0001. During training, the iteration and batch size in each epoch are always 1 since the whole image is directly input into the network, and the total training iteration number is set to 1K. The details of the proposed methods are shown in Table IV and the parameters are separately represents the “channel number”, “kernel size”, “stride”, “padding size” and “dilation rate” of the corresponding layer. In addition, the table also indicates whether the GN and ReLU are used after the convolutional layer. Besides standardization, we don’t adopt any data augmentation tricks in the proposed methods.

In the experiments, the training samples are obtained through randomly choosing, while the remainder consists of the validation set and testing set, where the accuracies are evaluated on the testing set. The validation set is used for model status monitoring during training. All experiments are repeated with 10 times, and we record the mean value in the later ablation studies. Three commonly used evaluation criterions in HSI classification community are applied in the experiments, including overall accuracy (OA), average accuracy (AA) and Kappa coefficient (Kappa). The OA is the most popular evaluation criteria, which is calculated through dividing the number of correct pixels by the number of pixels that need to be classified. However, the OA is usually affected by the phenomenon of unbalance categories. To tackle this problem, the AA and Kappa are separately computed based on the confusion matrix, where the recall values of all categories are averaged to get AA, while the Kappa is used to measure

TABLE IV
PARAMETER DETAILS OF THE PROPOSED METHODS

Part	Layer	Parameter	GN & ReLU
Backbone	Block1	64, 3, 1, 1, 1	✓
	Max Pool	64, 2, 2, 0, 1	
	Block2	128, 3, 1, 1, 1	✓
	Block3	256, 3, 1, 1, 1	✓
SAGR	ϕ, ψ, ρ, η	64, 1, 1, 0, 1	
	ξ, ζ	256, 1, 1, 0, 1	
SEGR	ϕ, ψ, ρ, η	$HW/64^1$, 1, 1, 0, 1	
	ξ, ζ	$HW/256$, 1, 1, 0, 1	
SAGR SEGR SSGR	δ	128, 1, 1, 0, 1 C_n^2 , 1, 1, 0, 1	✓

¹ Height and width of the feature F .

² Category number.

TABLE V
ACCURACIES WITH VARIOUS SETTING OF THE PROPOSED METHODS ON INDIAN PINES DATASET

Method	SAGR	SEGR	Auxiliary Branch	Multiple Loss	OA(%)	AA(%)	Kappa(%)
FCN				/	91.06	96.35	89.71
SAGR	✓	/		/	89.87	91.81	88.31
SAGR	✓	/	✓	/	94.04	95.66	93.11
SEGR	/	✓	/	/	95.64	97.88	94.97
SSGR	✓	✓			97.06	98.75	96.60
SSGR	✓	✓		✓	97.37	98.74	96.95
SSGR	✓	✓	✓	✓	97.87	98.77	97.52

the classification consistency to penalize the model possessing category preference. All experiments are implemented on the Intel Xeon Gold 5118 2.30GHz processor and a single NVIDIA Tesla V100 GPU.

C. Parameter Analysis

In the proposed methods, only the number of descriptors in SAGR and SEGR, which are exactly graph nodes number that separately determines the scale of spatial and spectral graph reasoning through the aggregating of the homogeneous regions or channels, are need to be configured manually. In view of this, we analyze the influence of the descriptor number on network accuracies, and the results are described in Figure 5. It can be apparently observed that the accuracies increase as the descriptor number growing. Concretely, the accuracies increase quickly in early stage, but the growth rate gradually slow down as the descriptor number further increasing, and the turning points are separately 4 and 32 in SAGR and SEGR, respectively. In addition, the accuracies keep it low when the spectral descriptors less than 16 because of the spectral information losing if a large amount bands are aggregated at once. In our experiments, in order to achieve high accuracies while reduce the computational complexity as much as possible, we set the descriptor number as 256 in both SAGR and SEGR.

D. Ablation Study

We evaluate the different parts of the proposed methods on Indian Pines dataset, including the branches of spatial or spectral graph reasoning (SAGR or SEGR) and the auxiliary branch in SAGR. In addition, the influence of multiple

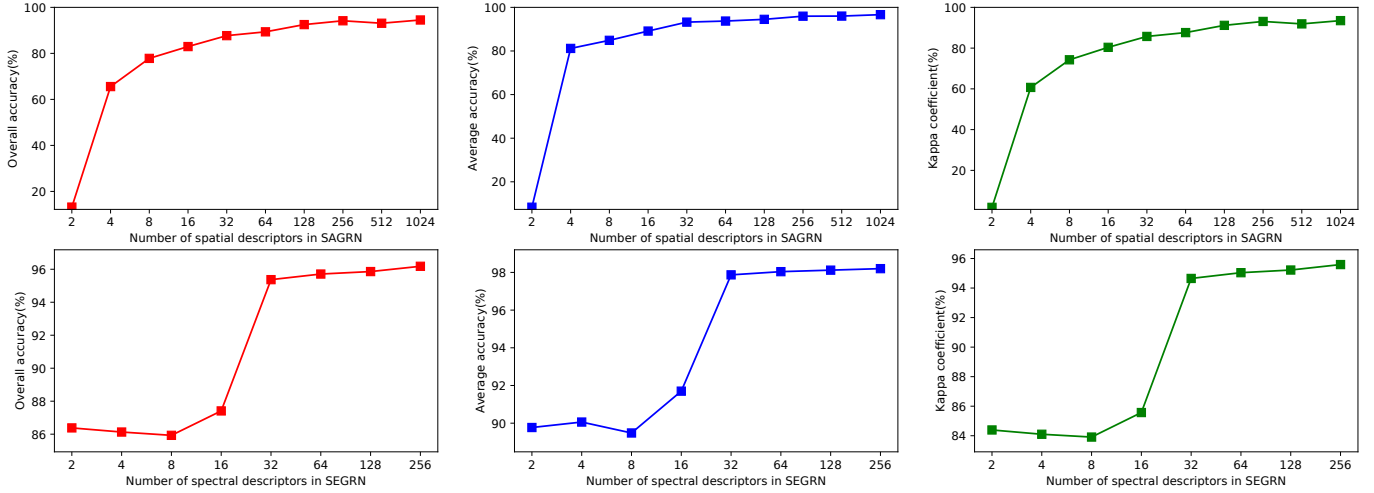


Fig. 5. Accuracies versus the descriptor number of SAGRN and SEGRN on Indian Pines dataset.

TABLE VI
MODEL COMPLEXITIES IN DIFFERENT COMBINATIONS OF THE PROPOSED METHODS ON INDIAN PINES DATASET

Method	Params(M)	FLOPs(G)	OA(%)	AA(%)	Kappa(%)
FCN	0.49	8.70	91.06	96.35	89.71
FCN+PAM	0.86	20.31	93.95	97.06	93.01
FCN+RCCA($R=2$)	0.86	16.00	93.40	95.38	92.38
FCN+SAGR	0.98	12.46	89.87	91.81	88.31
FCN+SAGR+AB	1.28	15.54	94.04	95.66	93.11
FCN+CAM	0.78	12.42	94.34	97.52	93.47
FCN+SEGR	1.09	12.00	95.64	97.88	94.97

TABLE VII
ACCURACIES VERSUS DIFFERENT TRAINING SAMPLE PERCENTS OF THE PROPOSED METHODS ON INDIAN PINES DATASET

Training sample (%)		100	80	60	40	20
SAGRN	OA	94.04	90.76	88.60	75.69	52.01
	AA	95.66	92.99	92.58	82.54	62.39
	Kappa	93.11	89.33	86.80	72.26	45.60
SEGRN	OA	95.64	94.07	92.95	88.45	82.17
	AA	97.88	97.39	97.06	93.15	87.56
	Kappa	94.97	93.16	91.86	86.76	79.58
SSGRN	OA	97.87	96.70	95.53	92.52	86.07
	AA	98.77	98.30	97.85	96.45	91.92
	Kappa	97.52	96.17	94.83	91.39	84.02

loss functions (we mainly consider the additional L_{sa} and L_{se} , while the L_{fused} is not included) is also considered, and the results are shown in Table V. It can be seen that the proposed methods improve the FCN a lot with the help of graph reasoning. However, without the auxiliary branch, the accuracies of SAGRN degrade seriously since the rough feature can't produce the high quality homogeneous areas and effective descriptors. The extra-added auxiliary branch directly supervises the corresponding feature rather than the reprojected feature like SAGR path, shortening the distance from the feature F to the classifier end, overcoming the phenomenon of difficult learning because of the weak gradient propagating, and further promoting the convergence of the network. Thus, the abilities of SAGR are helped to be more fully exploited with the high quality feature that generated under the aid of auxiliary branch and finally get better results.

Compared with FCN, the SEGRN performs better since the contextual information lying in different channels is well extracted by implementing the spectral graph reasoning, showing the importance of the abundant spectral information in HSI interpretation, which is a critical characteristic different from the natural image processing. By jointly taking advantage of the SAGR and SEGR, SSGRN achieves a better performance, especially with L_{sa} and L_{se} since the gradients gain a better propagation in corresponding SAGRN and SEGRN.

E. Model Complexity and Stability

In order to more comprehensively analyze the proposed methods, we assess the parameter number (Params) and computational complexity of SAGRN and SEGRN, while the latter is shown in the form of floating-point operations per second (FLOPs), and the results are shown in Table VI. Basing on the backbone network of FCN, we simultaneously compare the performance of the proposed SAGR and SEGR with other existing commonly employed non-local contexts capturing modules that utilize self-attention mechanism, including PAM [30], RCCA [32] and CAM [30], where the recurrent number R of RCCA is set to 2 to keep consistent with the original literature. It can be seen that our methods perform better than other modules since they achieve competitive accuracies with fewer computations. Concretely, for the square Indian Pines dataset, the inner product operations in PAM and recurrent RCCA are separately implemented N^2 and $4N\sqrt{N}$ times, while the proposed SAGR only needs $K^2 + NK$ times, where N is the pixel number of the input feature, K is the number of spatial descriptor, in practice $K \ll N$. In SEGRN, the complexity of SEGR is less than CAM since the feature F is downsampled before implementing graph reasoning. The "AB" in Table VI represents the auxiliary branch in SAGRN. Although the accuracies of FCN+PAM on Indian Pines dataset are close to FCN+SAGR+AB, it may not tackle some larger scenes such as the University of Houston dataset at one time due to the issue that out of memory, which unavoidably affects the classification. Actually, in our experiments, the

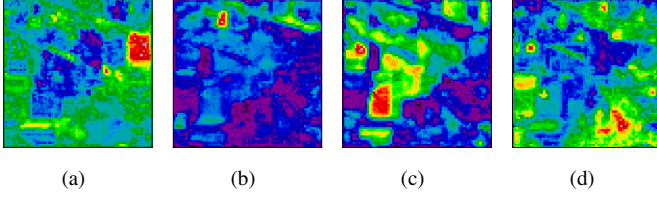


Fig. 6. Responsibility of different descriptors at each spatial position of feature F on Indian Pines dataset. The red color represents a high intensity. (a) Descriptor 1. (b) Descriptor 2. (c) Descriptor 3. (d) Descriptor 4.

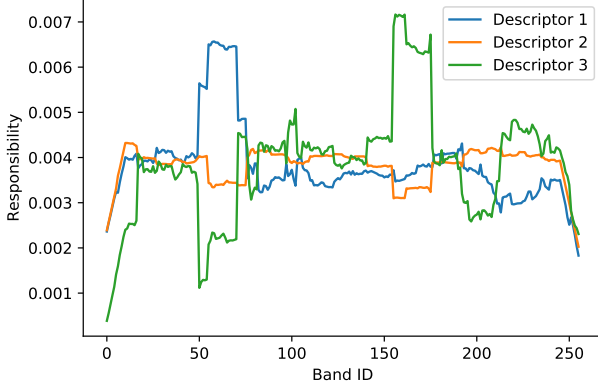


Fig. 7. Responsibility of different descriptors at each channel of feature F on Indian Pines dataset.

combination of FCN, SAGR and AB equals to SAGRN, while FCN+SEGR equals to SEGRN.

We also evaluate the stability of the proposed methods. Specifically, we separately adopt different percent of training samples of Table I, and the corresponding accuracies are shown in Table VII. It is obvious that the SEGRN is more robust than SAGRN since its OA higher than 80% even if only 20% of the training samples are available, while SAGRN drops almost half the accuracies. Nevertheless, by fusing the extracted spatial and spectral graph contexts, more than 90% of pixels are classified correctly in SSGRN when only 40% training samples are known, reflecting the stability of the proposed methods in the case of few samples.

F. Visualization

Besides the above quantitative analyses, to more intuitively understand our methods, we separately visualize the affinity matrix A of SAGRN and SEGRN, which indicates the similarities between the selected different descriptors with the vectors lying in different spatial positions or channels of the feature F , and the results are shown in Figure 6-7, where the responsibility intensity is represented with different colors or the height in direction of vertical axis. In Figure 6, it can be seen that different descriptors highlight different areas, demonstrating that they separately possess close relationships with the corresponding region. In other words, the connotations of these descriptors are certainly the meaning of the emphasized areas. These concepts serve as the basic components and can

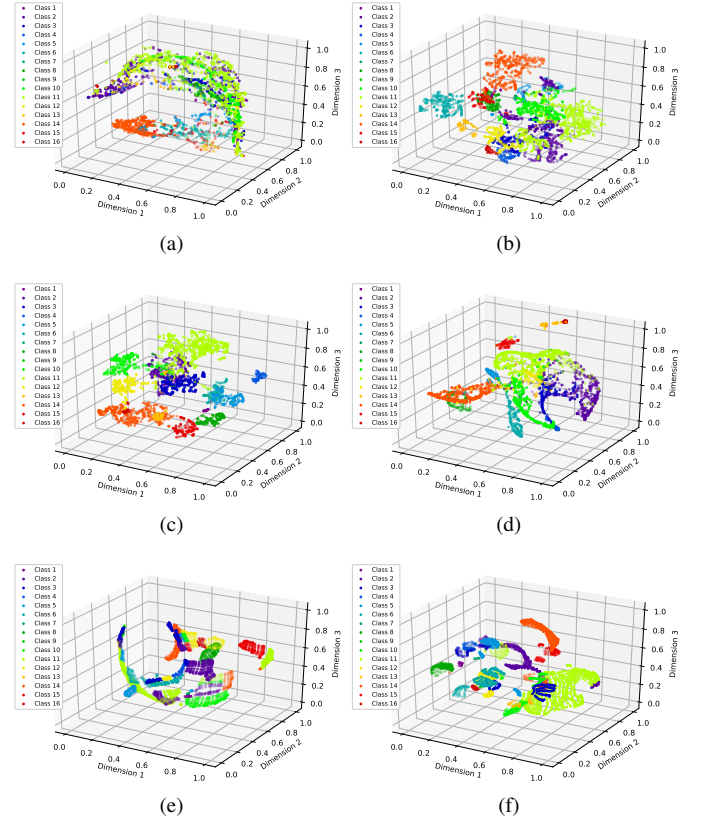


Fig. 8. Distribution of the reference samples at different feature spaces on Indian Pines dataset. (a) Input image. (b) Feature F . (c) Probability matrix P_{sa_aux} in SAGRN auxiliary branch. (d) The extracted feature F_{sa_main} in SAGRN main branch. (e) The extracted feature F_{se} in SEGRN. (f) The fused feature F_{fused} .

be organized by linearly aggregating the reasoned graph nodes in G to generate more complex semantic information for the understanding of other positions. While in Figure 7, different descriptors pay unequal attentions on each band. Thus, the responsibility curves have various shapes.

We also evaluate the distinguishability of the extracted features of the proposed SSGRN in a three-dimensional space by utilizing the t-SNE dimension reduction [57], where the distributions of reference sample at the corresponding input image, feature F generated by backbone network, probability matrix P_{sa_aux} of auxiliary branch, F_{sa_main} of SAGRN, F_{se} of SEGRN and the fused feature F_{fused} are separately shown in Figure 8. It can be observed that the samples on original image space are mixed-up and difficult to be identified, while after the encoding of backbone network, the obtained F began to be separable, and the auxiliary branch further strengthen the distinctions. Benefitting from the graph reasoning modules, the pixel representations on F_{sa_main} , F_{se} and F_{fused} possess high separability with large inter-class distances, and the points of each category constitute a unique manifold, indicating that the latent patterns of corresponding categories have been perceived, demonstrating the effectiveness of the proposed SSGRN.

TABLE VIII
ACCURACIES OF DIFFERENT ALGORITHMS ON INDIAN PINES DATASET (%)

Metric	1-DCNN	2-DCNN	SSFCN	GCN	Mini-GCN	MDGCN	CADGCN	SAGRN	SEGRN	SSGRN
OA	73.19±3.61	82.94±1.84	86.74±0.82	70.22±1.51	77.60±2.94	93.76±0.67	89.36±0.82	94.04±1.63	95.64±0.52	97.87±0.55
AA	83.29±2.12	92.88±0.83	92.87±0.94	79.00±1.20	76.93±1.79	91.60±1.10	93.24±1.01	95.66±1.99	97.88±0.27	98.77±0.19
Kappa	69.52±3.74	80.55±2.06	84.81±0.93	66.27±1.53	74.44±3.09	92.79±0.77	87.71±0.93	93.11±1.88	94.97±0.60	97.52±0.63
Class 1	86.92±7.73	99.23±2.31	99.23±2.31	76.15±9.39	76.92±8.41	100.00±0.00	95.38±2.15	92.31±4.25	100.00±0.00	99.23±0.31
Class 2	68.14±8.69	80.16±5.36	83.15±1.29	59.02±4.29	75.93±4.96	91.43±2.37	75.33±4.23	92.70±6.19	95.56±1.90	98.34±2.49
Class 3	66.70±9.11	89.67±4.51	91.15±1.80	64.68±4.84	51.64±9.91	92.52±1.67	87.18±3.54	95.21±2.41	96.30±2.03	96.58±1.18
Class 4	82.63±9.60	99.42±0.72	94.82±2.22	85.62±4.40	73.72±3.96	82.05±2.30	90.58±3.58	99.71±0.74	99.27±0.47	100.00±0.00
Class 5	92.22±2.35	93.97±3.84	94.93±0.95	88.64±3.52	92.92±1.88	91.46±2.10	91.62±2.69	98.43±1.13	94.26±1.49	98.17±1.14
Class 6	94.29±2.18	95.33±1.83	97.86±0.72	92.98±1.32	96.32±1.14	96.00±0.97	98.14±1.26	96.83±1.33	99.52±0.65	99.68±0.26
Class 7	93.75±8.39	100.00±0.00	97.50±5.00	91.25±8.00	62.50±9.41	83.33±5.76	95.00±5.09	87.50±3.67	100.00±0.00	100.00±0.00
Class 8	98.39±1.04	99.52±0.65	99.10±0.50	93.54±2.82	97.86±1.08	99.75±0.46	98.76±0.79	99.13±0.16	99.95±0.16	100.00±0.00
Class 9	86.67±6.33	98.33±5.00	95.00±7.64	68.33±8.93	0.00±0.00	77.78±6.01	100.00±0.00	100.00±0.00	100.00±0.00	100.00±0.00
Class 10	79.39±6.53	85.29±2.07	91.30±1.29	74.46±4.82	74.27±5.62	91.74±1.67	83.53±5.53	91.28±3.67	98.05±1.62	92.66±2.54
Class 11	56.92±8.31	64.34±4.42	74.82±1.52	53.18±8.12	71.21±9.58	92.88±1.74	88.99±3.73	90.32±2.17	92.70±1.45	97.71±2.07
Class 12	78.22±9.89	93.96±2.22	90.18±2.97	69.86±4.48	93.96±1.53	94.37±0.70	89.11±2.95	88.84±4.73	96.75±2.16	99.39±0.98
Class 13	98.10±2.92	99.90±0.29	99.90±0.29	97.24±1.31	99.14±1.21	94.21±0.84	99.71±0.44	99.71±0.67	100.00±0.00	100.00±0.00
Class 14	78.75±7.61	89.45±9.72	91.66±1.84	87.16±2.61	76.33±4.04	98.48±0.56	99.61±0.19	99.57±1.19	93.99±1.56	99.23±0.23
Class 15	74.97±9.39	98.57±1.12	88.11±1.81	70.17±3.46	98.11±1.31	98.37±0.26	98.95±1.49	97.55±0.87	99.65±0.23	98.60±0.42
Class 16	96.67±4.44	98.89±2.22	97.22±4.48	91.67±5.69	90.00±8.12	81.25±5.20	100.00±0.00	98.89±0.70	100.00±0.00	100.00±0.00

TABLE IX
ACCURACIES OF DIFFERENT ALGORITHMS ON PAVIA UNIVERSITY DATASET (%)

Metric	1-DCNN	2-DCNN	SSFCN	GCN	Mini-GCN	MDGCN	CADGCN	SAGRN	SEGRN	SSGRN
OA	75.39±2.49	89.19±1.01	89.91±0.68	81.83±2.26	83.40±2.44	94.23±0.69	92.08±2.66	94.79±1.33	88.91±3.04	98.04±0.42
AA	83.13±1.10	89.98±0.53	93.60±0.52	87.60±0.48	87.03±1.23	93.22±0.25	90.43±3.36	93.58±1.97	88.43±2.48	98.45±0.31
Kappa	68.73±2.60	84.49±1.27	86.84±0.88	76.75±2.62	78.61±2.96	92.40±0.90	89.64±3.27	93.06±1.77	90.88±3.86	97.39±0.56
Class 1	75.72±4.04	90.39±1.85	86.22±2.16	77.36±4.06	83.02±6.62	96.15±1.73	92.71±4.13	91.00±4.63	79.96±7.58	89.65±2.49
Class 2	70.17±7.07	88.59±2.30	87.09±0.89	77.35±5.19	82.45±5.77	93.44±1.56	93.85±4.03	98.52±1.39	88.63±3.28	99.92±0.27
Class 3	78.63±7.15	82.40±4.24	91.68±1.00	77.58±3.03	86.20±3.16	98.76±1.26	98.28±1.23	90.33±7.67	97.05±1.95	99.90±1.12
Class 4	92.82±4.76	92.03±1.35	96.65±0.63	93.74±2.55	93.17±3.16	83.51±1.78	84.98±4.79	90.18±5.82	70.55±4.08	99.16±0.50
Class 5	99.63±0.24	99.96±0.05	99.24±0.36	99.43±0.18	99.78±0.08	98.50±0.06	84.47±8.84	99.31±0.24	98.96±1.81	99.98±0.03
Class 6	71.50±8.59	76.24±5.06	92.88±1.25	87.32±4.26	96.31±3.22	99.46±0.49	95.31±6.30	98.85±2.07	99.76±1.91	98.50±0.45
Class 7	87.17±4.66	89.44±3.10	96.06±1.08	91.41±2.83	94.16±2.58	99.28±0.43	95.85±2.49	97.54±3.28	99.84±1.74	99.82±0.41
Class 8	72.64±8.72	91.53±2.31	92.96±0.93	84.43±2.98	48.29±9.79	95.41±1.10	82.59±5.91	80.28±8.25	95.51±3.50	99.30±1.03
Class 9	99.94±0.08	99.24±0.96	99.60±0.31	99.82±0.15	99.85±0.08	74.51±1.43	85.84±7.34	96.23±2.67	87.72±3.05	99.65±0.16

TABLE X
ACCURACIES OF DIFFERENT ALGORITHMS ON UNIVERSITY OF HOUSTON DATASET (%)

Metric	1-DCNN	2-DCNN	SSFCN	GCN	Mini-GCN	MDGCN	CADGCN	SAGRN	SEGRN	SSGRN
OA	80.23±0.84	84.08±1.18	94.60±0.38	85.73±0.95	83.51±1.86	91.58±0.43	91.78±0.68	92.38±1.94	89.87±1.52	95.59±1.95
AA	82.09±0.89	87.01±0.93	95.34±0.36	86.41±0.79	84.46±1.66	92.92±0.32	92.97±0.54	92.20±1.83	91.80±1.24	96.52±1.56
Kappa	78.61±0.91	82.77±1.28	94.16±0.41	84.54±1.03	82.15±2.01	90.89±0.46	91.10±0.74	91.75±2.10	89.04±1.63	95.23±2.11
Class 1	95.35±2.74	85.38±3.33	96.35±0.75	91.29±4.06	99.77±1.75	95.81±0.67	96.66±1.46	97.83±2.46	97.57±2.21	95.05±2.10
Class 2	97.20±2.55	75.06±5.27	97.49±0.49	98.20±1.17	81.77±4.17	79.64±1.88	73.17±2.81	96.19±6.35	93.59±2.83	94.71±2.63
Class 3	99.80±0.22	99.06±0.97	99.98±0.05	99.05±0.41	95.75±1.34	95.42±0.23	95.30±0.33	98.83±1.71	94.30±1.48	99.80±0.21
Class 4	94.20±3.09	77.73±5.20	96.94±0.76	96.20±2.60	91.41±1.92	77.17±2.69	83.36±2.15	85.23±4.21	89.34±4.92	97.90±2.58
Class 5	97.85±0.45	89.22±2.71	97.64±0.76	98.45±0.74	92.43±4.24	99.11±0.91	97.66±1.21	97.90±2.71	95.45±2.11	99.21±0.43
Class 6	95.87±3.64	97.51±1.96	95.11±1.58	96.84±1.68	98.84±2.35	97.11±1.16	96.47±1.10	86.67±4.25	98.67±0.93	99.69±0.98
Class 7	80.00±8.95	85.18±2.90	88.27±1.67	86.49±8.41	47.83±8.99	82.70±3.69	88.73±3.90	77.91±5.63	74.49±4.51	97.09±6.41
Class 8	46.56±5.55	70.53±4.77	93.88±1.05	69.17±4.66	85.54±6.04	94.44±3.39	88.21±4.71	92.66±3.74	77.53±4.27	96.50±4.44
Class 9	70.95±7.46	81.63±3.81	87.85±1.28	85.09±3.28	82.96±6.37	86.21±2.02	88.91±2.86	81.86±8.65	80.64±4.10	93.40±4.13
Class 10	70.23±8.22	88.34±2.26	95.39±1.22	71.63±8.77	89.61±5.25	96.34±1.31	98.47±0.85	93.70±6.20	95.39±5.63	87.84±3.28
Class 11	72.14±7.32	87.89±3.13	92.95±1.26	81.22±7.32	67.55±7.95	98.96±1.13	98.86±1.09	93.22±6.35	92.42±3.58	91.89±3.09
Class 12	57.49±9.06	74.49±3.78	91.88±0.93	69.39±6.46	90.61±5.58	93.51±1.06	92.89±2.03	97.18±4.31	87.56±2.85	94.17±4.31
Class 13	57.24±7.41	95.69±0.43	97.02±0.20	56.15±4.87	68.73±8.68	96.61±1.75	95.22±0.87	79.13±7.78	99.05±1.19	99.59±1.19
Class 14	98.32±0.82	99.76±0.56	99.91±0.20	98.14±0.79	92.16±2.06	100.00±0.00	100.00±0.00	98.78±1.41	99.94±0.18	100.00±0.00
Class 15	98.09±0.80	97.73±1.44	99.29±1.07	98.88±0.33	81.91±3.71	99.83±0.16	99.64±0.16	96.25±4.50	97.32±3.68	100.00±0.00

G. Performance Comparison

We conduct the comparison between the proposed methods with other state-of-the-art approaches, including the CNN-based networks: 1-DCNN [9] for spectral classification with the spectral vector, 2-DCNN [9] for spatial classification using the spatial patches, the FCN-based algorithm SSFCN [24] for spectral-spatial joint classification and the approaches on the foundation of graph convolution, including GCN [39], Mini-GCN [40], MDGCN [41] and CADGCN [42]. The implementation of GCN is in the pattern of transductive learning, where the whole image is directly fed into the

model since each pixel is regarded as a graph node, and it unavoidably consumes too much computing resource. Mini-GCN simplifies the problem by using a shrunk adjacency matrix that is obtained through computing only with the nodes in current mini-batch, while the graph nodes in MDGCN are obtained with the segmented superpixel and the classification is performed in superpixel-level, too. The CADGCN also uses the superpixels to generate the graph nodes and performs the pixel-region-pixel transformation.

Table VIII-X lists the classification accuracies of each algorithm, where the mean value and standard deviation are

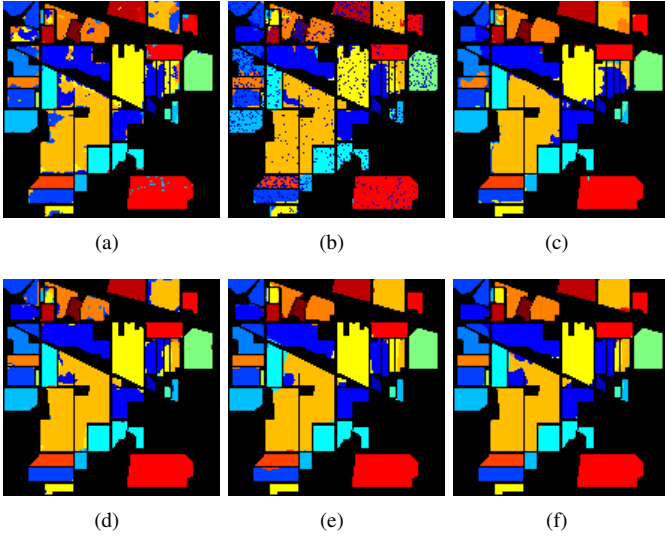


Fig. 9. Classification map of different methods on Indian Pines dataset. (a) SSFCN. (b) MDGCN. (c) CADGCN. (d) SAGRn. (e) SEGRN. (f) SSGRN.

simultaneously reported. It can be seen that the FCN-based SSFCN obviously perform better than the CNN-based 1-DCNN and 2-DCNN, showing the importance of spectral-spatial combination and large vision field in HSI classification. However, the accuracies of SSFCN are still limited because SSFCN only perceives the local information since its convolutions are all local operators. For the graph convolution-based methods, the redundant calculations of adjacent pixels in GCN affect the classification while Mini-GCN attempts to use the simplified adjacency matrix to accelerate this procedure with mini-batch training strategy. However, the pixels lacking of the representativeness of various contexts are directly set as the descriptors in GCN and Mini-GCN, degrading the classification. Some effective descriptors are obtained in MDGCN and CADGCN with the help of superpixel segmentation on the original image, thus they get higher accuracies than GCN and Mini-GCN. In addition, it needs to be noticed that the adjacency matrices in MDGCN and CADGCN are all calculated by only considering the relationships of neighbor nodes. Compared with the above methods, our SAGRn performs better since the more effective descriptors can be flexibly and adaptively generated through the homogeneous areas that are produced by implementing superpixel segmentation on the intermediate features of the network. Moreover, the SAGRn possesses the global view since the relationships between each node and all the other nodes are measured. By implementing the spectral reasoning, the SEGRn successfully captures the graph contexts lying in different channels. To our best knowledge, it is the first time that the relationships of spectral bands are perceived through graph convolution in HSI classification community. At last, combining the spatial and spectral graph contexts that are separately obtained by SAGRn and SEGRn, the proposed SSGRn performs the best and achieves the overall accuracy of 97.87%, 98.04% and 95.59% on Indian Pines, Pavia University and University of Houston dataset.

We select and predict the networks having relative higher accuracies shown in Table VIII-X, including SSFCN, MDGCN,

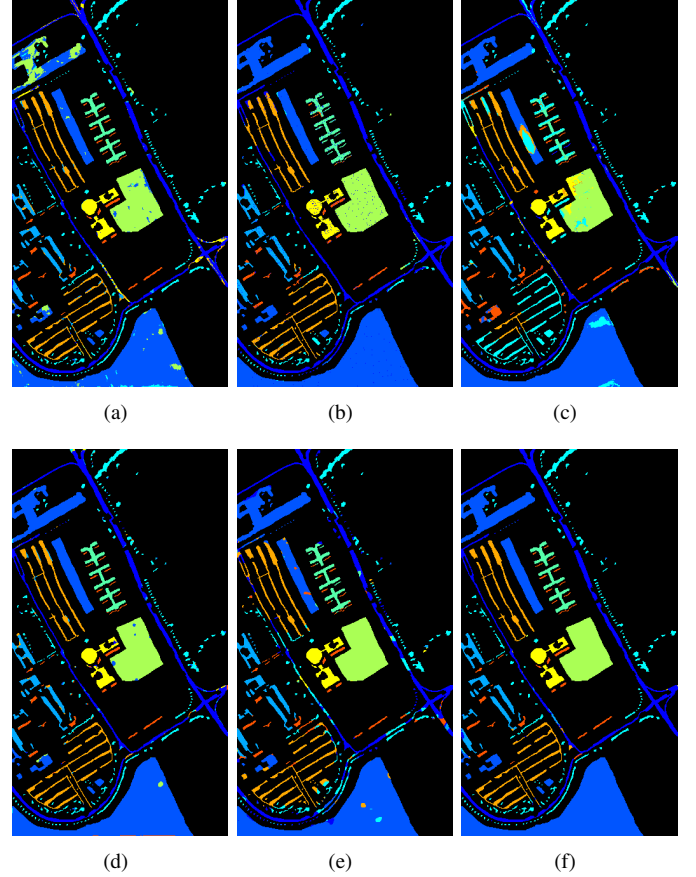


Fig. 10. Classification map of different methods on Pavia University dataset. (a) SSFCN. (b) MDGCN. (c) CADGCN. (d) SAGRn. (e) SEGRN. (f) SSGRN.

CADGCN and the proposed methods, and the results are depicted in Figure 9-11. It can be seen that the classification maps are consistent with the accuracies presented in Table VIII-X. We can obviously find that the proposed methods have fewer noises (compare with MDGCN) and misclassifications (compare with SSFCN and CADGCN), generating the discriminative classification maps where the objects possess continuous surfaces and well-maintained edges.

V. CONCLUSION

In this paper, we propose a network called SSGRn to classify the HSI. Considering that the irregular distribution of land objects and the various relationships of different spectral bands, the corresponding contextual information is more suitably extracted from the perspective of graph. Concretely, this network contains two subnetworks that separately extract the spatial and spectral graph contexts. In spatial subnetwork SAGRn, in order to generate the more effective descriptors for graph reasoning, different from the previous approaches implementing superpixel segmentation on the original image, we perform this procedure on the intermediate features inside network based on the pixel spectral-spatial similarities to more flexibly and adaptively produce the homogeneous regions and the descriptors are acquired through separately aggregating these regions. In addition, the SAGRn introduces less error

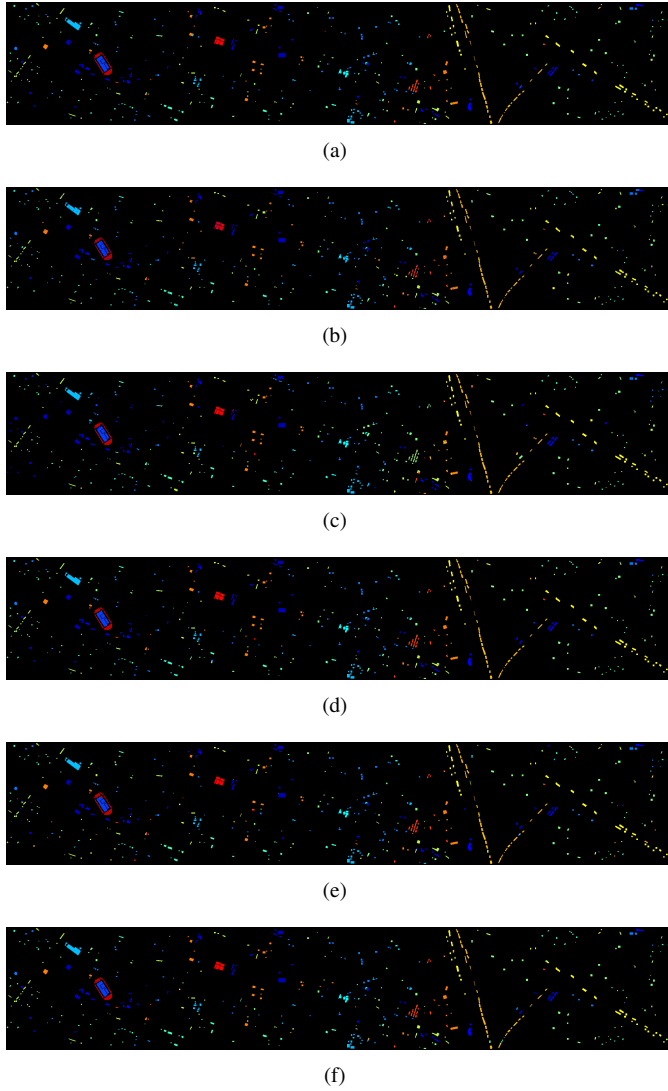


Fig. 11. Classification map of different methods on University of Houston dataset. (a) SSFCN. (b) MDGCN. (c) CADGCN. (d) SAGRN. (e) SEGRN. (f) SSGRN.

compared with other algorithms employing category features since all the homogeneous areas can be acquired automatically, especially in testing. What's more, we conduct a similar operation on channels to obtain the spectral graph contexts in spectral subnetwork SEGRN, where the spectral descriptors are gained by reasonably grouping the bands. To our best knowledge, it is the first time that the graph contexts lying in spectral bands are captured for HSI classification. The graph reasoning procedures in spectral and spatial subnetworks are all achieved with the graph convolution, where the adjacent matrices are obtained by computing the similarities of all the node pairs to guarantee the global perception, while the SSGRN is finally produced by combining SAGRN and SEGRN to further improve the classification. It needs to be noticed that the auxiliary branch and multiple loss strategy are separately applied in SAGRN and SSGRN to accelerate the convergence. A series of qualitative and quantitative comprehensive experiments show that the proposed methods can not

only maintain high accuracies but reducing the computational resource consumption and still perform stable with less training samples, while the performance comparison evaluations demonstrate the competitiveness compared with other state-of-the-art methods.

ACKNOWLEDGMENTS

The authors would like to thank Prof. Paolo Gamba and Prof. Saurabh for providing the Pavia University and University of Houston datasets. The numerical calculations in this paper have been done on the supercomputing system in the Supercomputing Center of Wuhan University.

REFERENCES

- [1] X. Zhang, Y. Sun, K. Shang, L. Zhang, and S. Wang, "Crop classification based on feature band set construction and object-oriented approach using hyperspectral images," *IEEE J. Sel. Topics Appl. Earth Observ. Remote Sens.*, vol. 9, no. 9, pp. 4117–4128, Sep. 2016.
- [2] X. Yang and Y. Yu, "Estimating soil salinity under various moisture conditions: An experimental study," *IEEE Trans. Geosci. Remote Sens.*, vol. 55, no. 5, pp. 2525–2533, May 2017.
- [3] S. Matteoli, M. Diani, and G. Corsini, "A tutorial overview of anomaly detection in hyperspectral images," *IEEE Aerosp. Electron. Syst. Mag.*, vol. 25, no. 7, pp. 5–28, 2010.
- [4] Y. Chen, Z. Lin, X. Zhao, G. Wang, and Y. Gu, "Deep Learning-Based Classification of Hyperspectral Data," *IEEE J. Sel. Topics Appl. Earth Observ. Remote Sens.*, vol. 7, no. 6, pp. 2094–2107, June 2014.
- [5] T. Li, J. Zhang, and Y. Zhang, "Classification of hyperspectral image based on deep belief networks," in *Proc. IEEE Int. Conf. Image Process. (ICIP)*, Oct 2014, pp. 5132–5136.
- [6] P. Zhou, J. Han, G. Cheng, and B. Zhang, "Learning compact and discriminative stacked autoencoder for hyperspectral image classification," *IEEE Trans. Geosci. Remote Sens.*, vol. 57, no. 7, pp. 4823–4833, 2019.
- [7] W. Hu, Y. Huang, L. Wei, F. Zhang, and H. Li, "Deep convolutional neural networks for hyperspectral image classification," *J. Sensors*, vol. 2015, 2015.
- [8] W. Zhao and S. Du, "Spectral-Spatial Feature Extraction for Hyperspectral Image Classification: A Dimension Reduction and Deep Learning Approach," *IEEE Trans. Geosci. Remote Sens.*, vol. 54, no. 8, pp. 4544–4554, Aug 2016.
- [9] Y. Chen, H. Jiang, C. Li, X. Jia, and P. Ghamisi, "Deep Feature Extraction and Classification of Hyperspectral Images Based on Convolutional Neural Networks," *IEEE Trans. Geosci. Remote Sens.*, vol. 54, no. 10, pp. 6232–6251, Oct 2016.
- [10] Z. Zhong, J. Li, Z. Luo, and M. Chapman, "Spectral-spatial residual network for hyperspectral image classification: A 3-d deep learning framework," *IEEE Trans. Geosci. Remote Sens.*, vol. 56, no. 2, pp. 847–858, Feb 2018.
- [11] L. Zhang, Q. Zhang, B. Du, X. Huang, Y. Y. Tang, and D. Tao, "Simultaneous spectral-spatial feature selection and extraction for hyperspectral images," *IEEE Trans. Cybern.*, vol. 48, no. 1, pp. 16–28, 2018.
- [12] Z. Feng, S. Yang, M. Wang, and L. Jiao, "Learning dual geometric low-rank structure for semisupervised hyperspectral image classification," *IEEE Trans. Cybern.*, vol. 51, no. 1, pp. 346–358, 2021.
- [13] Y. Xu, B. Du, F. Zhang, and L. Zhang, "Hyperspectral image classification via a random patches network," *ISPRS-J. Photogramm. Remote Sens.*, vol. 142, pp. 344–357, 2018.
- [14] Y. Xu, L. Zhang, B. Du, and F. Zhang, "Spectral-spatial unified networks for hyperspectral image classification," *IEEE Trans. Geosci. Remote Sens.*, vol. 56, no. 10, pp. 5893–5909, Oct 2018.
- [15] D. Wang, B. Du, L. Zhang, and Y. Xu, "Adaptive spectral-spatial multiscale contextual feature extraction for hyperspectral image classification," *IEEE Trans. Geosci. Remote Sens.*, pp. 1–17, 2020.
- [16] H. Sun, X. Zheng, X. Lu, and S. Wu, "Spectral-spatial attention network for hyperspectral image classification," *IEEE Trans. Geosci. Remote Sens.*, vol. 58, no. 5, pp. 3232–3245, 2020.
- [17] L. Mou and X. X. Zhu, "Learning to pay attention on spectral domain: A spectral attention module-based convolutional network for hyperspectral image classification," *IEEE Trans. Geosci. Remote Sens.*, vol. 58, no. 1, pp. 110–122, 2020.

- [18] R. Hang, Z. Li, Q. Liu, P. Ghamisi, and S. S. Bhattacharyya, "Hyperspectral image classification with attention-aided cnns," *IEEE Trans. Geosci. Remote Sens.*, pp. 1–13, 2020.
- [19] X. Tang, F. Meng, X. Zhang, Y. Cheung, J. Ma, F. Liu, and L. Jiao, "Hyperspectral image classification based on 3-d octave convolution with spatial-spectral attention network," *IEEE Trans. Geosci. Remote Sens.*, pp. 1–18, 2020.
- [20] M. Zhu, L. Jiao, F. Liu, S. Yang, and J. Wang, "Residual spectral-spatial attention network for hyperspectral image classification," *IEEE Trans. Geosci. Remote Sens.*, pp. 1–14, 2020.
- [21] H. Lee and H. Kwon, "Going deeper with contextual cnn for hyperspectral image classification," *IEEE Trans. Image Process.*, vol. 26, no. 10, pp. 4843–4855, Oct 2017.
- [22] M. Zhang, W. Li, and Q. Du, "Diverse region-based cnn for hyperspectral image classification," *IEEE Trans. Image Process.*, vol. 27, no. 6, pp. 2623–2634, 2018.
- [23] G. Cheng, Z. Li, J. Han, X. Yao, and L. Guo, "Exploring hierarchical convolutional features for hyperspectral image classification," *IEEE Trans. Geosci. Remote Sens.*, vol. 56, no. 11, pp. 6712–6722, 2018.
- [24] Y. Xu, B. Du, and L. Zhang, "Beyond the patchwise classification: Spectral-spatial fully convolutional networks for hyperspectral image classification," *IEEE Trans. Big Data.*, pp. 1–1, 2019.
- [25] Z. Zheng, Y. Zhong, A. Ma, and L. Zhang, "Fpga: Fast patch-free global learning framework for fully end-to-end hyperspectral image classification," *IEEE Trans. Geosci. Remote Sens.*, vol. 58, no. 8, pp. 5612–5626, 2020.
- [26] D. Wang, B. Du, and L. Zhang, "Fully contextual network for hyperspectral scene parsing," *IEEE Trans. Geosci. Remote Sens.*, pp. 1–16, 2021.
- [27] M. Zhang, W. Li, Q. Du, L. Gao, and B. Zhang, "Feature extraction for classification of hyperspectral and lidar data using patch-to-patch cnn," *IEEE Trans. Cybern.*, vol. 50, no. 1, pp. 100–111, 2020.
- [28] X. Wang, R. B. Girshick, A. Gupta, and K. He, "Non-local neural networks," *CoRR*, vol. abs/1711.07971, 2017.
- [29] A. Vaswani, N. Shazeer, N. Parmar, J. Uszkoreit, L. Jones, A. N. Gomez, L. u. Kaiser, and I. Polosukhin, "Attention is all you need," in *Proc. Adv. Neural Inf. Process. Syst. (NeurIPS)*, 2017, pp. 5998–6008.
- [30] J. Fu, J. Liu, H. Tian, Y. Li, Y. Bao, Z. Fang, and H. Lu, "Dual attention network for scene segmentation," in *Proc. IEEE Conf. Comput. Vis. Pattern. Recognit. (CVPR)*, 2019, pp. 3141–3149.
- [31] Y. Yuan and J. Wang, "Ocnet: Object context network for scene parsing," *CoRR*, vol. abs/1809.00916, 2018.
- [32] Z. Huang, X. Wang, L. Huang, C. Huang, Y. Wei, and W. Liu, "Ccnet: Criss-cross attention for semantic segmentation," in *Proc. IEEE. Int. Conf. Comput. Vis. (ICCV)*, 2019, pp. 603–612.
- [33] Z. Zhu, M. Xu, S. Bai, T. Huang, and X. Bai, "Asymmetric non-local neural networks for semantic segmentation," in *Proc. IEEE. Int. Conf. Comput. Vis. (ICCV)*, 2019, pp. 593–602.
- [34] H. Zhao, J. Shi, X. Qi, X. Wang, and J. Jia, "Pyramid scene parsing network," in *Proc. IEEE Conf. Comput. Vis. Pattern. Recognit. (CVPR)*, 2017, pp. 6230–6239.
- [35] Y. Yuan, X. Chen, and J. Wang, "Object-Contextual Representations for Semantic Segmentation," *arXiv e-prints*, p. arXiv:1909.11065, Sep. 2019.
- [36] F. Zhang, Y. Chen, Z. Li, Z. Hong, J. Liu, F. Ma, J. Han, and E. Ding, "Acfnet: Attentional class feature network for semantic segmentation," in *Proc. IEEE. Int. Conf. Comput. Vis. (ICCV)*, 2019, pp. 6797–6806.
- [37] S. Jia, Z. Lin, B. Deng, J. Zhu, and Q. Li, "Cascade superpixel regularized gabor feature fusion for hyperspectral image classification," *IEEE Trans. Neural Netw. Learn. Syst.*, vol. 31, no. 5, pp. 1638–1652, 2020.
- [38] J. Jiang, J. Ma, and X. Liu, "Multilayer spectral-spatial graphs for label noisy robust hyperspectral image classification," *IEEE Trans. Neural Netw. Learn. Syst.*, pp. 1–14, 2020.
- [39] T. N. Kipf and M. Welling, "Semi-supervised classification with graph convolutional networks," *CoRR*, vol. abs/1609.02907, 2016. [Online]. Available: <http://arxiv.org/abs/1609.02907>
- [40] D. Hong, L. Gao, J. Yao, B. Zhang, A. Plaza, and J. Chanussot, "Graph convolutional networks for hyperspectral image classification," *IEEE Trans. Geosci. Remote Sens.*, pp. 1–13, 2020.
- [41] S. Wan, C. Gong, P. Zhong, B. Du, L. Zhang, and J. Yang, "Multiscale dynamic graph convolutional network for hyperspectral image classification," *IEEE Trans. Geosci. Remote Sens.*, vol. 58, no. 5, pp. 3162–3177, 2020.
- [42] S. Wan, C. Gong, P. Zhong, S. Pan, G. Li, and J. Yang, "Hyperspectral image classification with context-aware dynamic graph convolutional network," *IEEE Trans. Geosci. Remote Sens.*, pp. 1–16, 2020.
- [43] J. Long, E. Shelhamer, and T. Darrell, "Fully convolutional networks for semantic segmentation," in *Proc. IEEE Conf. Comput. Vis. Pattern. Recognit. (CVPR)*, 2015, pp. 3431–3440.
- [44] O. Ronneberger, P. Fischer, and T. Brox, "U-net: Convolutional networks for biomedical image segmentation," *CoRR*, vol. abs/1505.04597, 2015.
- [45] V. Badrinarayanan, A. Kendall, and R. Cipolla, "Segnet: A deep convolutional encoder-decoder architecture for image segmentation," *IEEE Trans. Pattern Anal. Mach. Intell.*, vol. 39, no. 12, pp. 2481–2495, 2017.
- [46] H. Noh, S. Hong, and B. Han, "Learning deconvolution network for semantic segmentation," in *Proc. IEEE. Int. Conf. Comput. Vis. (ICCV)*, 2015, pp. 1520–1528.
- [47] G. Lin, A. Milan, C. Shen, and I. Reid, "Refinenet: Multi-path refinement networks for high-resolution semantic segmentation," in *Proc. IEEE Conf. Comput. Vis. Pattern. Recognit. (CVPR)*, 2017, pp. 5168–5177.
- [48] C. Yu, J. Wang, C. Peng, C. Gao, G. Yu, and N. Sang, "Learning a discriminative feature network for semantic segmentation," in *Proc. IEEE Conf. Comput. Vis. Pattern. Recognit. (CVPR)*, 2018, pp. 1857–1866.
- [49] C. Peng, X. Zhang, G. Yu, G. Luo, and J. Sun, "Large kernel matters - improve semantic segmentation by global convolutional network," *CoRR*, vol. abs/1703.02719, 2017.
- [50] C. Yu, J. Wang, C. Peng, C. Gao, G. Yu, and N. Sang, "Bisenet: Bilateral segmentation network for real-time semantic segmentation," in *Proc. Eur. Conf. Comput. Vis. (ECCV)*, V. Ferrari, M. Hebert, C. Sminchisescu, and Y. Weiss, Eds. Cham: Springer International Publishing, 2018, pp. 334–349.
- [51] H. Zhang, K. Dana, J. Shi, Z. Zhang, X. Wang, A. Tyagi, and A. Agrawal, "Context encoding for semantic segmentation," in *Proc. IEEE Conf. Comput. Vis. Pattern. Recognit. (CVPR)*, 2018, pp. 7151–7160.
- [52] L. Chen, G. Papandreou, F. Schroff, and H. Adam, "Rethinking atrous convolution for semantic image segmentation," *CoRR*, vol. abs/1706.05587, 2017.
- [53] M. Yang, K. Yu, C. Zhang, Z. Li, and K. Yang, "Denseaspp for semantic segmentation in street scenes," in *Proc. IEEE Conf. Comput. Vis. Pattern. Recognit. (CVPR)*, 2018, pp. 3684–3692.
- [54] D. K. Hammond, P. Vandergheynst, and R. Gribonval, "Wavelets on graphs via spectral graph theory," *Appl. Comput. Harmon. Anal.*, vol. 30, no. 2, pp. 129 – 150, 2011. [Online]. Available: <http://www.sciencedirect.com/science/article/pii/S1063520310000552>
- [55] R. Achanta, A. Shaji, K. Smith, A. Lucchi, P. Fua, and S. Süsstrunk, "Slic superpixels compared to state-of-the-art superpixel methods," *IEEE Trans. Pattern Anal. Mach. Intell.*, vol. 34, no. 11, pp. 2274–2282, 2012.
- [56] V. Jampani, D. Sun, M.-Y. Liu, M.-H. Yang, and J. Kautz, "Superpixel sampling networks," in *Proc. Eur. Conf. Comput. Vis. (ECCV)*, September 2018.
- [57] L. van der Maaten and G. Hinton, "Visualizing data using t-sne," *J. Mach. Learn. Res.*, vol. 9, no. 86, pp. 2579–2605, 2008. [Online]. Available: <http://jmlr.org/papers/v9/vandemaaten08a.html>